The International Journal of Advanced Manufacturing Technology
https://doi.org/10.1007/s00170-025-15064-2

ORIGINAL ARTICLE

Prediction of electrohydrodynamic printing behavior using machine learning approaches

Yizhou Lu[1] · James Treadway[1] · Prashant Ghimire[1] · Yiwei Han[1] · Samrat Choudhury[1]

Received: 4 September 2024 / Accepted: 13 January 2025

Abstract
Electrohydrodynamic (EHD) printing has been used in various applications (e.g., sensors, batteries, photonic crystals). Currently, research on studying the relationships between EHD jetting behaviors, material properties, and processing conditions is still challenging due to a large number of parameters, cost, time, and the complex nature of experiments. In this research, we investigated EHD printing behavior using a machine learning (ML)-guided approach to overcome limitations in the experiments. Specifically, we investigated two jetting modes and the size of printed material with a broader range of material properties and processing parameters. We used samples from both literature and our own experiment results with different type of materials. Different ML models have been developed and applied to the data. Our results have shown that ML can navigate a vast parameter search space to predict printing behavior with an accuracy of higher than 95% during EHD printing. Moreover, the results showed that ML models can be used to predict the printing behavior and feather size for new materials. The ML models can guide the investigation of EHD printing and helped us understand the printing behavior in a systematic manner with reduced time, cost, and required experiments.

Keywords Machine learning · Prediction · Electrohydrodynamic printing · Additive manufacturing

1 Introduction

Additive manufacturing (AM) has revolutionized the way of production as it is capable of direct fabrication of highly complex structures, which can be challenging or impossible with traditional manufacturing approaches [1, 2]. Different types of AM processes have been developed (e.g., stereolithography, powder bed fusion, directed energy deposition) for a range of applications [3, 4], such as aerospace, automative, and healthcare. Among all the AM processes, high-resolution additive manufacturing processes are critical for many applications [1, 5, 6]. Inadequate manufacturing accuracy and surface finish in many current AM methods significantly limits their application in producing high-precision components. For example, printing of transparent electronics requires a feature resolution of less than 10 μm [7, 8]; AM of optical devices also requires high precision [9]. A printing process capable of achieving micro-scale resolution can not only reduce fabrication time and cost, but also simplify post-processing as well.

Electrohydrodynamic (EHD) printing is an emerging printing technique capable of producing micro- or nano-resolution products using a range of materials [10]. Compared with other high-resolution manufacturing techniques, such as laser-based process [11], photolithography [12], high-resolution material jetting [13, 14], and two-photon polymerization [15], EHD printing is an inexpensive, versatile, and highly customizable alternative for creating precision components with sub-micron resolutions. Polymer solutions, metals, nanomaterials, biomaterials, and phase-change materials have been used in EHD printing for applications such as micro 3D structures, flexible electronics, and scaffolds [10]. In EHD printing, ink is

✉ Samrat Choudhury
schoudhu@olemiss.edu

Yizhou Lu
ylu3@go.olemiss.edu

James Treadway
jmtread1@go.olemiss.edu

Prashant Ghimire
pghimir1@go.olemiss.edu

Yiwei Han
yhan2@olemiss.edu

[1] Department of Mechanical Engineering, University of Mississippi, University, MS 38677, USA

Published online: 29 January 2025

subjected to an electric field (Fig. 1a) to form a Taylor-cone, and a droplet or jet is generated at the tip of the cone (Fig. 1b). Various EHD printing modes (dripping mode, microdripping mode, spindle mode, multispindle mode, cone-jet mode, oscillating-jet mode, precession mode, ramified jet, etc.) have been identified based on forms and dynamics of the meniscus/jet and forms of liquid emitted. Two printing modes, microdripping mode and cone-jet mode, stand out in particular for being able to produce stable fabrications with high precision. In microdripping mode (Fig. 2a), fine droplets can be printed and precisely deposited on a substrate, while cone-jet mode (Fig. 2b) is capable of producing a single fine stable filament [16].

Understanding the mechanisms and interactions between the EHD printing process and material properties can provide good insights that can help improve the printing process, optimize feature resolution, and identify new materials. Extensive research has been conducted in order to understand the EHD printing process and its relationship with different material properties. A vast number of experimental tests have been conducted to study relations between process parameters, printing behavior, and feature dimensions for various materials [17–19]. However, this process requires tremendous amounts of time and cost due to the intricate multiphysics involved in EHD printing. Therefore, both theoretical and simulation models have been developed to study mechanisms of EHD printing, as well as accelerated determination of processing-property linkage. For example, Lee's group created phase diagrams and jetting maps to qualitatively show the relationship between printing modes and two critical printing parameters, voltage and flow rate [20]. Some groups have utilized the scaling law to study the relation between printing process parameters (i.e., minimum flow rate, electric fields, surface charge density) and printed features under pulsating mode and cone-jet conditions [21–26]. Several groups have also applied numerical methods to study droplet size and charge in EHD printing, and they found that droplet size and charge is affected by ink conductivity and several scaling regimes [27–30]. Droplet-substrate interaction has also been studied using numerical methods. Pannier's group utilized the spherical cap

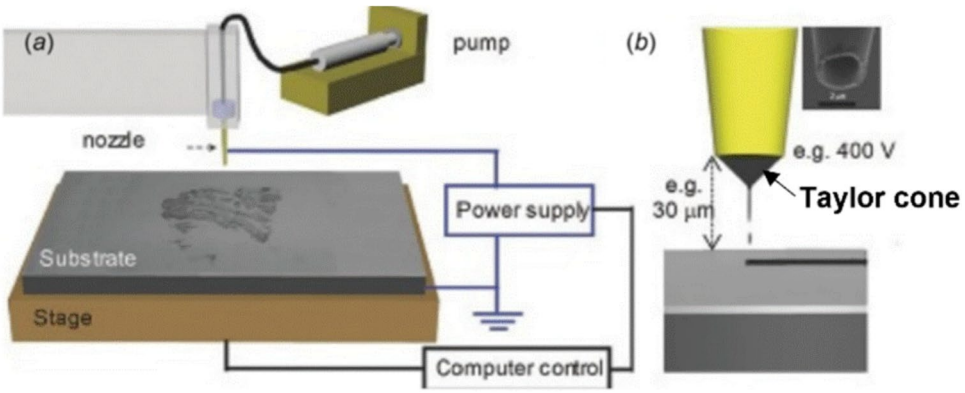

Fig. 1 High-resolution EHD printing: **a** schematic illustration of an EHD printing system. **b** Typical nozzle and substrate configuration for EHD printing [10]

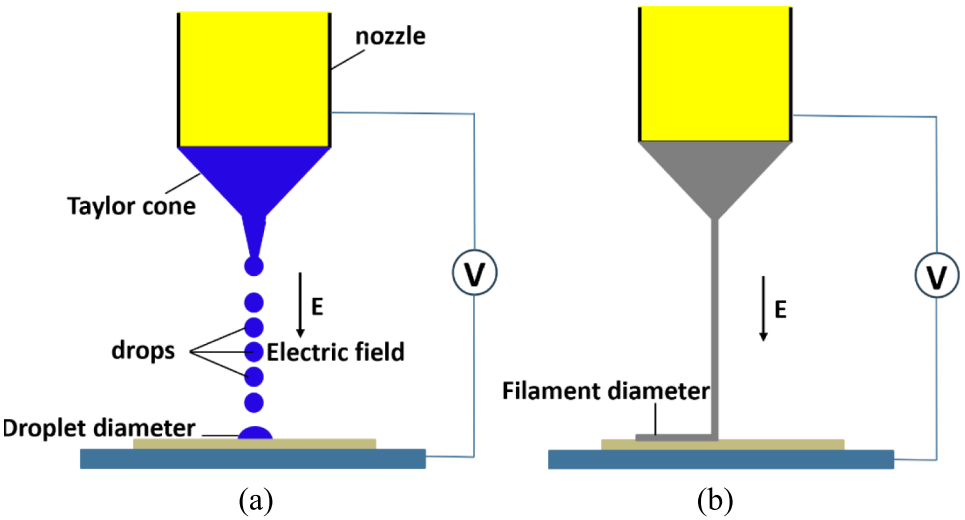

Fig. 2 Schematic of printing modes: **a** microdripping mode; **b** cone-jet mode

volume conservation law and molecular kinetics to study droplet spreading substrates [31]. The mentioned models have provided valuable insights into how the EHD printing process interacts with different material properties, and several dimensionless numbers have been created for predicting the printing mode. However, those models primarily focus on creating dimensionless numbers to describe the interaction of printing process and material properties. As a result, those models are not able to provide a good prediction of feature dimensions. Some groups have developed different simulation models to predict droplet or jetting size. For instance, Du's group developed a finite element approach (FEA) model to study droplet breakup at cone tips, as well as droplet size and mass by integrating voltage, charged species, and two-phase flow [32]. Dong's group developed an FEA and computational fluid dynamics (CFD) model for studying EHD microdripping mode printing, and their developed models were able to predict droplet inflight velocity, droplet size, and final footprint [33, 34]. Zeshan and Yanqiao's groups developed FEA models to simulate the EHD cone-jet and microdripping mode printing process using different design parameters, which was later validated by experiments [35, 36]. Nevertheless, these models usually possess limitations, in that they are typically tailored towards one specific material or one particular printing behavior, which is difficult to adopt in unknown scenarios. Consequently, they can only provide limited insights into the realm of EHD printing, and offer limited guidance in the field of future parameters and material selection. Currently, a model that can accurately describe and predict EHD printing which can be generalized for a wide range of materials has not been established.

To develop such a model, we propose a more recent approach based on machine learning (ML) in this study, which can contribute a novel perspective in the field of EHD printing. ML is a data-driven method that studies the wealth in existing data, and can potentially lead to a paradigm shift in the way traditional research is conducted. Using data and information from existing samples, ML models can be trained to further explore the nature of research targets, which may not be possible to extract using conventional research methods. ML can also assist in predicting research targets, which offers opportunities to operate research in a more economical direction with high fidelity.

ML has been applied to study EHD printing in previous research. For example, some studies utilize supervised ML methods to establish the relations between printing process parameters and product dimension and performance, which can improve manufacturing efficiency [37, 38]. Supervised ML methods have also been applied with images in order to investigate the relation between process parameters and printing modes [39, 40]. Athanasios' group developed an end-to-end physics-informed machine learning framework to study the mechanism of the EHD jetting process with reduced experiment cost [41]. All of those studies utilized data from their experiments with limited materials and process conditions. However, all processing parameters must be studied comprehensively in order to determine their combined effects on printing product quality. Furthermore, such models have not been subjected to external validation through experiments conducted by other researchers. Sachin's group has collected data from relevant publications and used it for training ML models [42]. The developed models can determine the importance of different parameters that affect the printing results. However, it's worth noting that this research relied on an extensive external dataset to increase model accuracy, and the applicability of the developed model for new materials has not been validated. Here, we perform a ML-based research on the relationship between a comprehensive combination of parameters and printing behavior using data from both internal and external sources for a vast number of materials. By evaluating parameter importance and building models for predicting printing behavior, we investigate each parameter related to printing behavior in a more systematic manner and the mechanism of EHD printing process is studied more thoroughly compared to previous research. Moreover, by validating the developed ML model for new materials, which was not explored in preceding work, the stress related to the cost, time consumed, and experiments required in conventional EHD printing research is relieved effectively.

In this work, we have applied the ML tools to study the interaction between EHD printing parameters and material properties, and how those parameters affect the jetting mode and the diameter of printed material. With these created ML models, important parameters that play a vital role in EHD printing have been identified. The generated models have exhibited the ability to accurately predict printing behavior and printed feature resolutions, which has been validated by our dataset with reduced time cost by a factor of 8 compared with FEA simulation. Furthermore, we have demonstrated the capacity of our developed model for the precise prediction of the jetting mode and diameter of printed product materials not included in the training dataset. These results underscore the potential of utilizing such developed models for predicting printing performance with new materials, and minimizing the need for actual experimentation.

2 Methods

2.1 Data collection

The data used in this work comes from two distinct sources: data generated from our own experiments and experimental

data extracted from external publications. More than 100 previously reported articles regarding droplets and filaments during EHD printing were consulted. To characterize printing behavior, two factors were considered in this work: jetting mode (forms of printed material) and diameter of printed materials. To maintain consistency among the dataset, we excluded publications which did not include one or more printing parameters and material properties such as electric field (V/μm), pressure (Psi), printing speed (mm/s), viscosity (mm^2/s), surface tension (mN/m), density (g/cm^3), printing temperature (°F), and nozzle size (μm) as well as the jetting mode and printed feature diameter (μm). The publications used in this project are listed in the reference [43–53]. Only average values of the printing parameters collected from the above references are used in this study. For our experimental data, the printing behaviors and dimensions were directly captured and measured from a high-resolution camera and optical microscope, and average values from our data are used in this study. The viscosity, surface tension, and density of the materials were obtained using a rotational viscometer, tensiometer with pendant drop methods, and a high-precision scale. To comprehensively encompass the pertinent materials associated with EHD printing, we meticulously selected four distinct material categories: phase change ink (wax and PCL), nanomaterials ink (silver nanowire ink (AgNW) and silver nanoparticle ink (AgNP)), and molten metal (Field's metal) and polymer solutions (poly(3,4-ethylenedioxythiophene):polystyrene sulfonate (PEDOT:PSS), polystyrene (PS), poly(methyl methacrylate) (PMMA), glycerin, and mixture of glycerin, as well as water and sodium chloride (NaCl)). Table 1 presents a detailed breakdown of these materials and their material properties, printing parameters, jetting mode, and diameter of printed materials, all of which were applied in this research. It is important to note that only data produced with DC voltage is included in this study, and all features are printed in the perpendicular direction. Besides the physical properties discussed in this paper, the conductivity of the material also has a significant impact on printing behavior [54, 55]. However, only a few papers include all the selected features (parameters which may affect the target in ML) and material conductivity. To ensure that the number of samples was sufficient for ML work, electrical properties were not incorporated in the ML models. Substrate surface wettability also plays a role in determining feature size. All substrates used in this work have a hydrophilic surface, but the exact surface energy or substrate material is not specified in several references. In this work, the substrate is not considered as a feature in developing the ML model. The datasets include two parts: the input features ($x: x_1, x_2, x_3, \ldots. x_n$) and one output target (y), which depends upon said input features. The input features, output target and sample size for each dataset is presented in Table 2. The diameter of printed droplet (Fig. 2a) or filament (Fig. 2b) on the substrate after printing represents the diameter of printed material in this work.

2.2 Data processing and machine learning model development

2.2.1 Dataset training

To train ML models for predicting the jetting mode and diameter of printed materials, the entire collected dataset is split into a training set and a test set in an 80:20 ratio. The training set is applied to optimize the model by minimizing

Table 2 The input features, output target and sample size in each dataset

Dataset no.	Input features (X)	Output target (Y)	Sample size
1	$X_1, X_2, X_3, X_4, X_5, X_6, X_7$	Y_1	109
2	$X_1, X_2, X_3, X_4, X_5, X_6, X_7, X_8$	Y_2	73
3	$X_1, X_2, X_3, X_4, X_5, X_6, X_7$	Y_3	54

Table 1 A detailed breakdown for materials in the dataset

Materials	Materials properties (X)	Printing parameters (X)	Jetting mode (Y)	Diameter of the printed materials (Y)
AgNP [43] AgNW [44, 45] Field's metal [46–48] Glycerin Mixtures of glycerine, water and NaCl Wax [46] PCL [49] PEDOT:PSS [50–52] PMMA [53] PS [53]	Surface tension (X_1) Viscosity (X_2) Density (X_3)	Electric field (X_4) Pressure (X_5) Nozzle size (X_6) Printing temperature (X_7) Printing speed (X_8; only for filament)	Filament Droplet (Y_1)	Diameter of filament (Y_2) Diameter of droplet (Y_3)

the loss function, while the test set is for evaluating the model performance.

In addition to the train-test split discussed above, we also investigated the potential of applying ML models in predicting the printing behavior and feature size for new material. For each ML model, all of the samples belonged to one or two selected printed materials were kept as the test set, while the rest of the samples were regarded as the training set.

2.2.2 Data scaling

The training set collected from the publications and experiments contains various units and ranges, which will prevent the ML model from learning the relationship between features and targets. Therefore, data scaling is applied to reduce the bias of feature units and ranges on model training. In this research, the training set was scaled by standardization.

The formula of the standard scaler is as follows:

$$x_{\text{new}} = \frac{x - \mu}{\sigma} \tag{1}$$

x_{new}: the data after scaling
x: original data
μ: mean value within the feature
σ: standard deviation within the feature

Since the test set is predicted by ML model as an unknown space, the mean value (μ) and standard deviation (σ) for scaling the test set are inherited from the training set.

2.2.3 Random forest (RF)

Feature importance analysis studies the effects of features on predicting a target. It scores the relationship between the features and the target to determine which features which show a robust relationship with the target, and reject the features that exhibit a weak relationship with the target. By this analysis, material properties and printing parameters in Table 1 that play a significant role in EHD printing can be identified as important features, which affects the jetting mode and the diameter of printed material.

In this research, random forest [56–58] is applied to the collected dataset as the feature importance analysis tool. Compared to other common feature importance analysis tools (F-value, mutual information, Pearson's correlation coefficient, bi-directional elimination), random forest is better suited to probe nonlinear relationships between features, analyzing features numerically, as well as minimizing the overfitting issue.

Random forest is composed of hundreds of decision trees (Fig. 3b). A decision tree is a non-parametric supervised learning technique that can be applied to both categorical and numerical targets. Random forest constructs a tree-like structure, created by splitting data based on decisions under different conditions.

A decision tree is composed of the following: (a) a root node where dataset enters the decision tree; (b) a decision node to divide the income data into its sub-nodes; and (c), a leaf node as the final node to export data that arrives at this node (Fig. 3a).

The workflow of a decision tree contains four steps:

Step 1: Input the data into the decision tree at the root node.
Step 2: Split the data into sub-nodes (decision node or leaf node) according to the criterion made by attribute measure techniques.
Step 3: If the sub-node is a decision node, repeat step 2. Otherwise, output the data that reaches the leaf node.
Step 4: Once all data is output at the leaf nodes, end the algorithm of the decision tree.

In step 2, several popular techniques can be utilized in deciding the best attribute for the root node and decision node when it comes to splitting the data. In this research, regression (numerical target) mean square error (MSE) is used, while Ginni index (GI) is applied for classification (categorical target). The two techniques are explained mathematically in Eqs. (2) and (3) [58].

$$\text{MSE} = \frac{1}{n}\sum_{i=1}^{n}\left(\hat{y}_i - y_i\right)^2, \tag{2}$$

where n is the total number of observations, $\hat{y}_i$ is the ith predicted target, and y_i is the ith true target.

$$\text{GI} = 1 - \sum_{i=1}^{c} p_i^2, \tag{3}$$

where p_i is the proportion of the samples in class c for a particular node.

In random forest, each decision tree is built by both a random extraction of observations, and a random extraction of features from the dataset. This random extraction guarantees that the trees are de-correlated, and avoids the overfitting problem.

In each decision tree within the random forest, feature importance is calculated based on node importance:

$$F_{\text{jk}} = W_k C_k - W_{\text{left}(k)} C_{\text{left}(k)} - W_{\text{right}(k)} C_{\text{right}(k)} \tag{4}$$

F_{jk} = the importance of node k for feature j
W_k = weighted number of samples reaching node k
C_k = the impurity value of node k (calculated by MSE in regression and GI in classification)
left(k) = child node from left split on node k
right(k) = child node from right split on node k

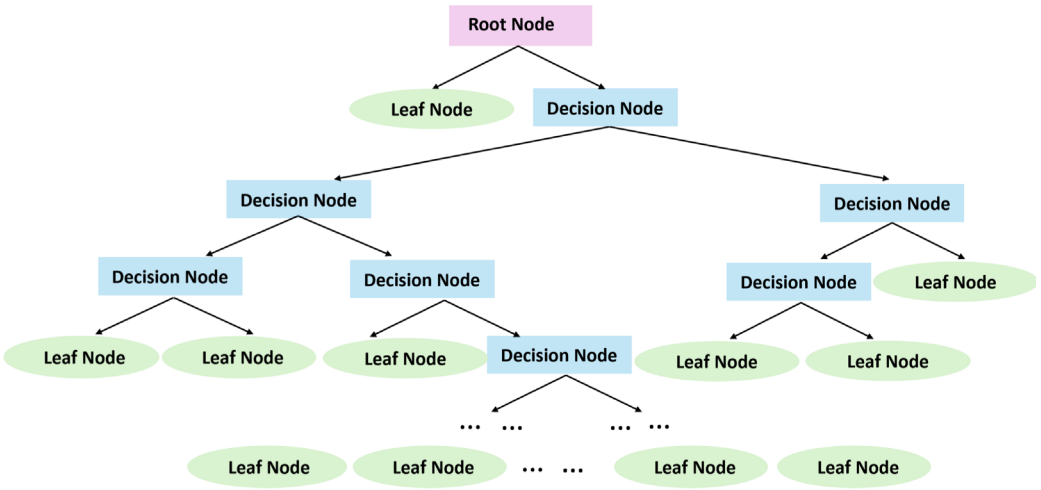

(a)

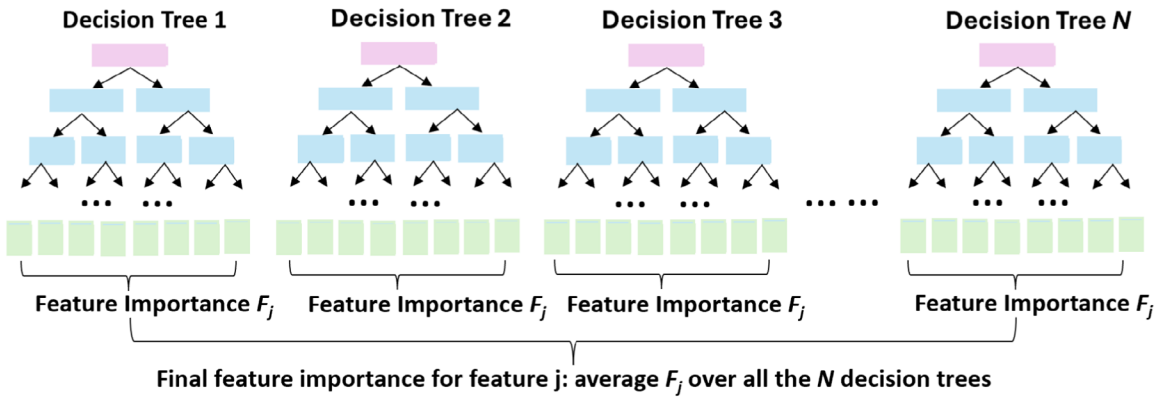

(b)

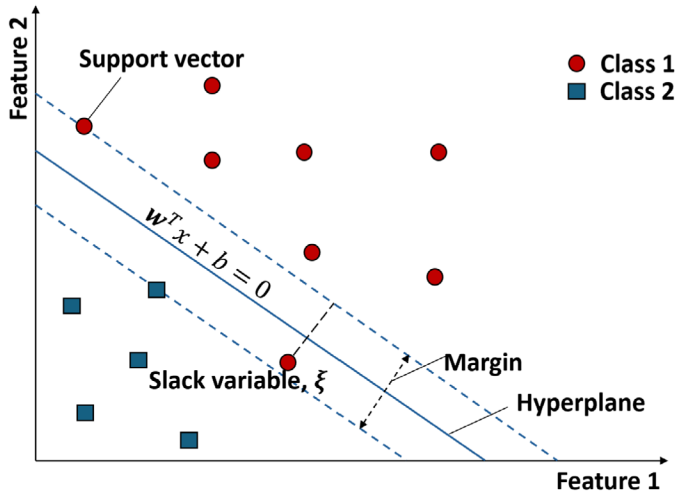

(c)

Fig. 3 Schematic explanation of ML models applied in this work. **a** Components in decision tree (DT); **b** random forest (RF); **c** support vector machine (SVM) with two features

For feature importance in each decision tree:

$$F_j = \frac{\sum_{k:\text{node } k \text{ splits on feature } j} F_{\text{jk}}}{\sum_{h\in\text{all nodes}} F_{\text{jh}}} \tag{5}$$

F_j = the importance of feature j
F_{jk} = the importance of node k for feature j
F_{jh} = the importance of node h for feature j

The final feature importance for each decision tree is normalized by dividing by the sum of all feature importances. In random forest, feature importance is the average value over all decision trees. Higher feature importance represents a stronger link between the feature and the target.

Another feature importance analysis technique using decision trees is extra trees. In extra trees, the whole dataset is applied to each decision tree. However, in random forest, it subsamples the input data with bootstrap. In addition, random forest selects the optimal node to split, whereas extra trees chooses the split randomly. Thus, extra tree is worse than random forest when the dataset contains noisy features. For this research, due to the uncertainty of feature importance within domain knowledge, random forest was determined as the most useful feature importance analysis method for this study.

In this research, three random forests were trained to analyze the importance of features controlling the jetting mode, diameter of filament and diameter of droplet, respectively. Hyperparameters of random forest (number of decision trees, minimum number of samples at the leaf node) were tuned by grid search.

2.2.4 Support vector machine (SVM)

Support vector machines (SVM), based on the Vapnik-Chervonenkis (VC) theory, was initially introduced by Boser (1992) and Vapnik (1995) as a binary classification technique [59, 60], and it has thrived in the ML-assisted engineering and science area in the past few years [61–63]. We employed SVM in this work for its efficient performance in high dimensional space. Additionally, a clear margin is exploited in SVM to help the model generalize more effectively than other frequently used classifiers (such as logistic regression, k-nearest neighbors (KNN), and decision trees).

In SVM, a decision boundary separates two classes using a hyperplane in the feature space. Margin, defined as the distance between the hyperplane and the observations closest to it, is vital in SVM. The mathematics of support vector machine learning allows the classification to not only classify data, but to find the optimal separator. It searches for a separator that maximizes the distance between the nearest data point of each group (Fig. 3c).

In this paper, the jetting mode can be either a droplet or filament, which defines the prediction of the jetting mode as a binary classification. In an SVM classifier for binary classification, a hyperplane is developed to separate the samples into the two classes. The dataset is defined as $\{x_i, y_i\}$, where i=1, 2, …, n. x_i is the feature vector for ith sample and y_i is its true class [64]. Later, the hyperplane can be mathematically described as follows:

$$\boldsymbol{w}^T x + b = 0 \tag{6}$$

where $\boldsymbol{w}$ is the weight vector that is perpendicular to the hyperplane and b is a constant offset from the origin.

While several hyperplanes can split the data into two classes, SVM classifiers investigate the hyperplane which handles the trade-off between minimizing classification errors and maximizing the margin that separates the two classes. Two normalizations clarify a hyperplane where the closest points are distributed on opposite sides of the hyperplane (Eq. (7) and Eq. (8)).

$$\boldsymbol{w}^T \boldsymbol{x}_+ + b = 1 \tag{7}$$

and

$$\boldsymbol{w}^T \boldsymbol{x}_- + b = -1 \tag{8}$$

The distance between Eq. (7) and Eq. (8) is calculated as follows:

$$d = \left(x_+ + x_-\right) \bullet \frac{\boldsymbol{w}}{\|\boldsymbol{w}\|} = \frac{2}{\|\boldsymbol{w}\|} \tag{9}$$

To maximize the margin, SVM classifier minimizes $g(w)$, defined as follows:

$$g(w) = \frac{1}{2}\|\boldsymbol{w}\|^2 \tag{10}$$

In reality, classification is often interrupted by outliers. To improve the flexibility of SVM in classification with noise or outlier issues, ξ, the slack variable, is added to the algorithm to tolerate misclassifications caused by such noise or outliers. Thus, Eq. (10) can be rewritten as follows:

$$g(w, \xi) = \frac{1}{2}\|\boldsymbol{w}\|^2 + C\sum_{i=1}^{n} \xi_i \tag{11}$$

where C is the regularization parameter that controls the training loss of misclassified data.

Then:

$$y\left(\boldsymbol{w}^T \boldsymbol{x}_i + b\right) \geq 1 - \xi_i, \quad \xi_i \geq 0 \tag{12}$$

The solution to the hyperplane is generated by Lagrange duality and quadratic optimization [64]. In some ML cases using SVM, linearly separable patterns are ineffective for classification. Therefore, in these cases, the original data is mapped to a higher feature space for accurate separation

of data via kernel functions based on dot products of two feature vectors. In SVM, many kernels can be utilized for nonlinear cases (polynomial kernel, radial basis function (rbf) kernel, etc.).

In this paper, the SVM classifier is applied to predict the jetting mode (filament vs. droplet). Dataset 1 described in Table 2 is the input into the SVM classifier. The hyperparameters of SVM (regularization parameter, kernel function, degree of kernel function, etc.) were tuned using grid search and cross-validation.

2.2.5 Kernel ridge regression (KRR)

Kernel ridge regression is one of the most popular ML techniques for regression. As a combination of ridge regression and kernel function, the nonlinear function to elaborate the link between features and the numerical target is distinctly explored in a higher dimensional space compared to the original space and KRR has been successfully applied for many engineering applications [65–67]. Besides the popularity of KRR in the field of engineering, a neat closed-form solution as well as a high work efficiency are also notable benefits of the application of KRR in this paper.

In KRR [68, 69], the dataset is set up as: $\{x_i, y_i\}$, where $i = 1, 2, \ldots, n$; x_i is the feature vector for ith sample and y_i is its true numerical target. The prediction function of KRR is as follows:

$$\hat{y}_j = \sum_{i=1}^{n} w_i \boldsymbol{K}(x_i, x_j) \tag{13}$$

where $\hat{y}_j$ is the jth predicted target, w_i are the weights to be optimized, and $\boldsymbol{K}(x_i, x_j)$ is the kernel function which clarifies a set of pairwise similarity comparisons between the training samples. Linear relationships are one of the easiest functions to understand. However, in practice, for certain cases a purely linear function is not a precise formulation. Therefore, we used kernel function to better trace the behavior of the data points in a higher dimensional space. Like SVM, several kernel functions are popular in KRR (polynomial kernel, radial basis function (rbf) kernel, sigmoid kernel, etc.). The loss function of KRR to develop the model is expressed as follows:

$$\text{Loss} = \sum_{i=1}^{n} \left(\hat{y}_i - y_i\right)^2 + \lambda \|\boldsymbol{w}\| \tag{14}$$

where $\hat{y}_i$ is the ith predicted target, y_i is the ith true target, and λ is a hyperparameter to describe the regularization strength. The first term in Eq. (14) is to evaluate the errors between the true target and the prediction from KRR, while the second term represents the penalty of a large w_i, which may cause overfitting. In KRR model training, Eq. (13) is minimized to explore the optimal w_i. Combining the minimization and kernel function effects, $\boldsymbol{w}$ can be expressed as follows:

$$\boldsymbol{w} = (\boldsymbol{K} + \lambda \boldsymbol{I})^{-1} \boldsymbol{y} \tag{15}$$

where $\boldsymbol{K}$ is the kernel matrix, and $\boldsymbol{I}$ is the identity matrix.

We used KRR models for predicting the diameter of printed materials in this work. Datasets 2 and 3 in Table 2 were used to train the model. Cross-validation was applied during the grid search for hyperparameters in the KRR models (regularization parameter, kernels, etc.).

2.3 Evaluation metrics

The performance of each classification model was rated by accuracy, and each regression model was scored by coefficient of determination (R^2), mean absolute error (MAE), and root mean square error (RMSE). Accuracy is defined as the ratio of the number of all correct predictions to the total number of predictions. R^2 is determined by the difference between the true value and the predicted value, as well as the difference between the true value and the mean value. Therefore, it can represent how strong the data fits the model. MAE represents the average of the absolute differences between true and predicted values, and also the average of the residuals. RMSE was used to calculate the rooted average of the squared difference between the true value and predicted values, which describes the variance of the residuals.

The formula for each evaluation metric is listed below:

$$\text{Accuracy} = \frac{\text{Number of correct predictions}}{\text{Number of all predictions}}, \tag{16}$$

$$R^2 = 1 - \frac{\sum_{i=1}^{n} \left(y_i - \hat{y}_i\right)^2}{\sum_{i=1}^{n} \left(y_i - \bar{y}_i\right)^2}, \tag{17}$$

$$\text{MAE} = \frac{1}{n} \sum_{i=1}^{n} \left|\hat{y}_i - y_i\right|, \tag{18}$$

$$\text{RMSE} = \sqrt{\frac{1}{n} \sum_{i=1}^{n} \left(\hat{y}_i - y_i\right)^2}, \tag{19}$$

where n is total number of observations, $\bar{y}_i$ is the mean value of the target, $\hat{y}_i$ is the predicted target, and y_i is the true target. All these models utilized in our machine learning work were implemented in Scikit-learn packages.

3 Results

3.1 Feature importance analysis

In this section, we outline the importance of individual features as well as the capability of the ML-based model in predicting printing behavior. The predictive target is composed of both the jetting mode and the diameter of printed material. In this work, the features (x_i) used in the ML to determine the printing behavior (y) are printing parameters (electric field strength, printing temperature, pressure, and nozzle size) and properties of materials (viscosity, surface tension, and density). The same features were also selected for predicting the diameter of the droplet. To predict the diameter of the filament, one additional feature, printing speed, was applied to the ML work, as the diameter of the filament is directly related to printing speed. A higher printing speed will result in a thinner filament, while a slower speed will produce a thicker filament.

The feature importance analysis was able to extract important feature that had notable effects on the printing behavior, which provides insight into the mechanisms of the EHD printing process and simplifies the model to describe printing behavior. The random forest models applied to the feature importance analysis are summarized in Supp. Table 1 in the supplemental information section. The relative importance of feature in determining the jetting mode (droplet or filament) is evaluated by random forest as presented by Fig. 4a. A feature with a higher importance value represents a stronger link between the feature and the jetting mode, indicating that the feature plays a more vital role in jetting mode determination. From the results, viscosity is ranked as the highest among the analyzed features in determining jetting mode. The viscosity of a fluid is measured by its resistance to gradual deformation, and more external influence will be needed to deform or alter the shape/movement of a fluid with a higher viscosity. In EHD printing, the length of the jet is directly proportional to its viscosity. When the viscosity is sufficiently high (>100 cP), the molecular attraction between the ink molecules is strong, resulting in more stable jets during EHD printing. In contrast, for low-viscosity fluids (<100 cP), the weaker attraction between the surfactants leads to the formation of microdrops. Thus, a continuous jet or filament will tend to form with highly viscous fluid instead of droplets during the printing process [69]. In EHD printing, a fine jet or drop is collected from the tip of the Taylor cone once the electrostatic force overcomes the surface tension and the viscous force of the printed material. If the surface tension is too low, the ink will form satellite droplets before a stable jet can be created, due to a longer pinch-off time (the time it takes for a droplet to detach from the jet). Studies also indicate that if the surface tension is too high, the applied electrostatic force will be insufficient to initiate jetting, leading to only meniscus pulsing and no printing [18, 70]. Therefore, the electric field (which generates the electrostatic force) and the surface tension of the material also play significant roles in determining jetting mode (Fig. 4a). Another important feature determined by this feature importance analysis is material density, as it is closely related to surface tension. Moreover, higher molecular weight for polymeric materials tends to create a higher viscosity, and higher molecular weight generally results in higher density [71, 72]. Compared to the features discussed above, printing temperature, pressure, and nozzle size do not exert significant influence in determining jetting mode compared to viscosity, surface tension, density, and electric field. This is because printing temperature, pressure, and nozzle size are processing conditions, while viscosity, surface tension, and density are material properties. Generally, material properties are known to determine jetting behavior more than processing conditions.

The feature importance in predicting the diameter of droplets is ranked from high to low in Fig. 4b. Both nozzle size and pressure play very important roles in controlling droplet diameter. Surface tension and electric field are also critical in determining droplet diameter. However, compared with the result from Fig. 4a, the importance of the electric field and surface tension is relatively diminished. This indicates that pressure is more a important feature than the electric field, which is consistent with Wang's work which finds pressure to be more critical than electric field in determining droplet diameter [73]. An interesting finding is that printing temperature ranks as the second most crucial feature in this analysis. This may be attributed to the limited number of droplet data points at different printing temperatures. Most of the droplets have diameters larger than 30 μm, and are printed around room temperature. But, only one material, wax, is printed at very high temperature (230°F) with small diameters (less than 30 μm), which makes the temperature variance among the droplets large. We hypothesize that this causes the machine to identify temperature as an important feature.

Figure 4c presents the relationship between each feature and the diameter of filament. In contrast to the droplet diameter, density and electric field affect the filament diameter much more than other features, while nozzle size and pressure are among the least important features for determining filament diameter. The distinct results from Fig. 4b and c originate from the difference in material properties that determine the formation of the droplet or filament. Generally, filaments are easily generated with materials with higher viscosities. Thus, viscous force plays a more critical role than surface tension, which is directly correlated with nozzle size. Furthermore, the flow rate of high viscosity materials is also less sensitive to pressure changes; hence,

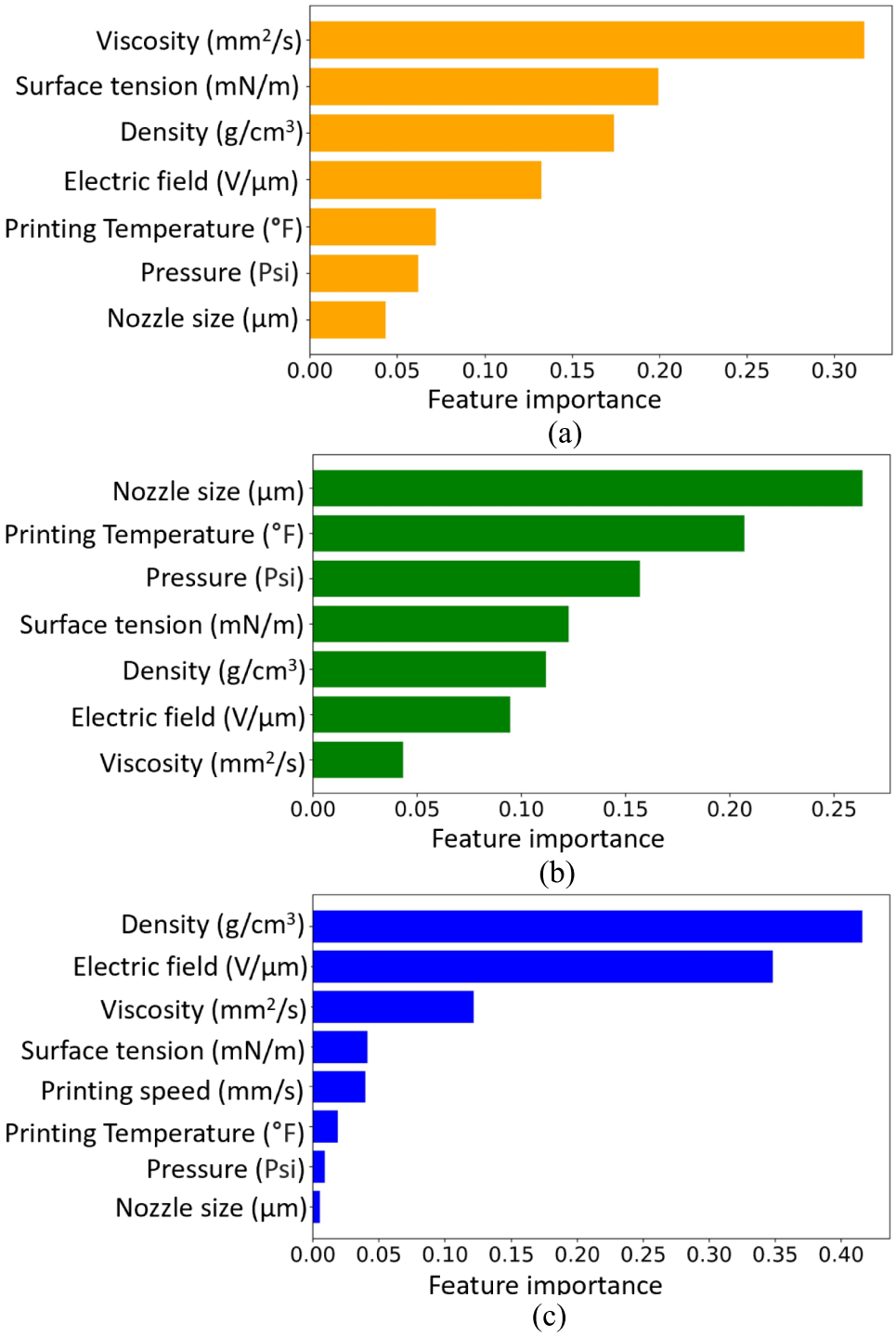

Fig. 4 Feature importance analysis. **a** Classification (droplet or filament); **b** regression (diameter of droplet); **c** regression (diameter of filament)

filament diameter is less sensitive to variations in nozzle size and pressure. In EHD printing, the flow rate, which directly determines the size of the filament, also depends on the applied electric field, as the electrostatic force applied on the meniscus will generate a suction effect [74]. Ahn's group performed a dimensionless analysis of mapped EHD jetting modes [20]. One of the findings from that research is that the critical flow of the jet is inversely proportional to only one parameter: material density, and that material density can also affect jetting diameter. Our results further supported their findings that density is a critical feature in determining filament diameter.

By the feature importance analysis, it was demonstrated that the ML model approach advances our understanding of the physical mechanisms behind EHD printing behavior under different jetting modes. Traditionally, it is believed

that jetting modes are primarily determined by three factors: viscosity, surface tension, and electric field. However, our results indicate that other factors are also important. For instance, density plays a crucial role in determining the jetting mode and influencing the filament diameter.

3.2 ML for classification and regression

In the EHD printing process, controlling the parameters for targeted printing behavior is based on trial and error, which is quite costly and time-consuming. Thus, ML is an excellent solution to this issue. The result of predicting the jetting mode (droplet vs. filament) via an SVM model is depicted as a confusion matrix in Fig. 5a. The hyperparameters used in this SVM model are presented in Table 2 in the Supplemental Information of this paper, and all hyperparameters in our models were determined by minimizing RMSE. In the dataset, the input features (x_i) are listed in Fig. 4a, and the output target (y) represents the printing behavior. In Fig. 5a, the jetting modes of 28 samples from the test set were predicted by the SVM model trained by the training set. Jetting modes were predicted correctly in 27 samples, while one sample was misclassified. The misclassified data is from the AgNW sample, which has only one data point in the entire sample set for classification. Moreover, one feature (printing speed, 8 mm/s) value of the AgNW data falls outside the range (1–6 mm/s) within the training set, which makes AgNW more challenging for the ML to predict. The accuracy of this SVM model is 96.43%, which shows that the developed ML model can provide a high accuracy when predicting the jetting mode. Moreover, the robust model performance further strengthens the comprehensive relationship between the input features and the jetting mode. In order to eliminate any bias in the random nature of our test samples, we repeat the experiment in Fig. 5a, with six separate sets of random train-test splits to validate the SVM model. Our results show an accuracy ranging from 96.43 to 100% (see Supp. Fig. 1 in Supplemental Information). These results demonstrate that the high accuracy of our SVM model is not an artifact of our choice of test samples. Time required for each prediction using the SVM model is approximately 30 min, which is a significant reduction compared to 4–6 h of time needed for a typical FEA simulation as observed in one of our previous works [33]. Hence, besides lowering the experimental cost in study EHD printing behavior, this ML approach accelerates EHD printing predictions.

In EHD printing, the product quality is closely related to the resolution of the printer, which can be determined by the diameter of the printed material. The predicted droplet diameter using the KRR model is presented in the form of a scatterplot in Fig. 5b. In this figure, the x-axis is the true diameter from the experiments, while y-axis is the predicted diameters by ML. The dashed parity line is the equation

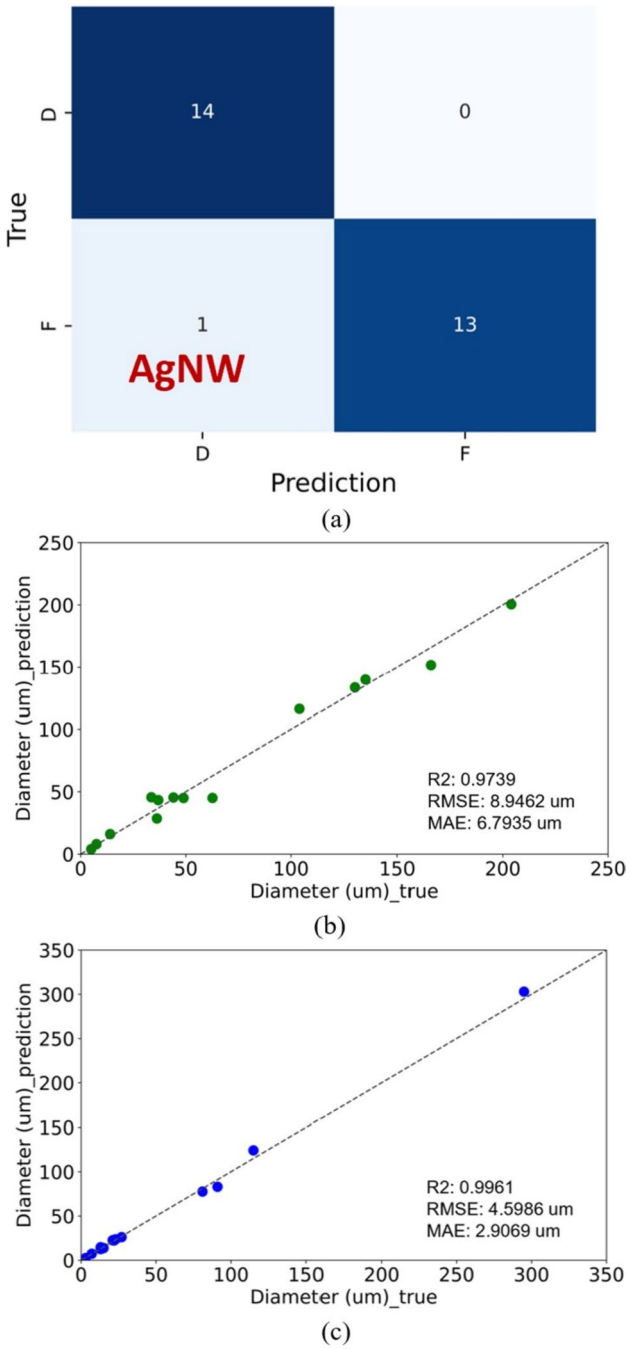

Fig. 5 ML predictions using random train and test split. **a** Classification (droplet or filament); **b** regression (diameter of droplet); **c** regression (diameter of filament)

where $y = x$, representing perfect model performance. R^2, RMSE, and MAE are generated to evaluate the model performance. In Fig. 5b, all samples are scattered around the parity line with an R^2 as high as 0.9739. Additionally, the result has no outliers, which highlights the efficiency of the KRR model in predicting droplet diameter. The performance of the KRR model for predicting filament diameter

is presented in Fig. 5c. All test samples fit the parity line well with a R^2 of 0.9961. The R^2 is positively related to the model prediction capability, which illustrates a greater model performance in the filament case compared to the droplet case. Additionally, RMSE (4.5986 μm) and MAE (2.9069 μm) of the KRR model in Fig. 5c are smaller than the RMSE (8.9462 μm) and MAE (6.7935 μm) in Fig. 5b, which similarly depicts better model performance in filament diameter prediction than droplet diameter prediction. The differing model performances likely originate from the distribution of data in the original dataset. There were 73 filament samples generated in our sample set, while only 54 droplet samples were gathered in the droplet sample set. The ML tool is known to be crucially influenced by dataset size. Increased sample size provides more information during the ML training process, and increases prediction accuracy. Lack of information may have influenced the droplet case, as the total number of droplet samples is 26.03% less than the number of filament samples.

To further validate the prediction capability of KRR models for predicting the diameter of printed materials, six other random train-test splits were performed in both droplet and filament samples (see Supp. Fig. 2 and 3 in Supplemental Information). All results demonstrated a consistently high accuracy (R^2 in droplet case = 0.9220–0.9862, and R^2 in filament case = 0.9614–0.9868) when predicting the diameter of printed materials using the KRR model. It is interesting to observe that although the data points for droplet and filament diameter were obtained for a range of materials from a wide range of sources (literature vs. our own experimental data), the accuracy in predicting the diameter is greater than 97%, indicating the robust nature of the KRR model. Further details on the KRR models used to predict the diameter of printed materials can be found in Supp. Table 3 of the Supplemental Information.

3.3 ML for predicting printing behavior of new materials

Different materials exhibit various printing behaviors. But, not all of these behaviors are desirable for every application. For example, the printing of filament is better suited for fabricating scaffolds or conductors, while droplet printing is preferable for creating complex 2D and 3D patterns. Accurately predicting how specific materials react to printing conditions enables us to select suitable materials and reduces the necessary time and cost for experiments. Moreover, it can also further the development of novel functional materials using fewer experiments. To predict the printing behavior of new materials, PMMA (droplets) and AgNP (filaments) are selected as representative novel materials. Among them, both PMMA and AgNP samples are obtained from reported literature. We ensured that the values of each feature for the samples from the two materials within the test samples fall within the range of values of the features in the training set, as the training set should cover enough information to predict the test set. Thus, PMMA and AgNP are ideal test set candidates, considering the representation of data sources, jetting modes, and the reasonability of the feature space. The predicted jetting modes in the test set are exhibited in Fig. 6a. It's noted that the predicted test set in Fig. 5 includes varying materials and processing parameters, while material properties are kept fixed in Fig. 6, and only the process conditions vary in test samples. For a test set of 20 samples, only one misclassified sample, which was from the PMMA sample with the lowest electric field (3.33 V/μm), was observed. This misclassification may be due to the presence of PEDOT:PSS sample. According to Fig. 4a, viscosity, surface tension, density, and electric field are the four most important parameters in deciding the jetting modes. There is only one PEDOT:PSS sample (viscosity: 46.88 mm^2/s; surface tension: 41.8 mN/m; density: 1.011 g/cm^3; electric field: 2.5 V/μm), and it shares similar orders of magnitude in viscosity, surface tension, and density as the PMMA (viscosity: 22 mm^2/s; surface tension: 30.5 mN/m; density: 0.879 g/cm^3) sample. For all other samples, their orders of magnitude in viscosity, surface tension, and density are notably different from PMMA. For example, PCL has viscosity of 181,000 mm^2/s, surface tension of 30.8 mN/m, and density of 1.145 g/cm^3. Moreover, the lowest electric field among the PMMA samples (3.33 V/μm) is very close to that applied to the PEDOT:PSS sample. The model may have labeled the PMMA sample with the lowest electric field as PEDOT:PSS, which forms the filament during the printing. Nonetheless, the accuracy of this model is 95.24%, which implies that the model is capable of predicting the jetting mode of new materials. This SVM model for predicting the jetting mode of new materials is described in Supp. Table 2 in Supplemental Information.

The prediction of the printed PMMA diameter serves as an example of diameter prediction using a KRR model for new materials in the droplet case (Fig. 6b). All five samples are positioned along the parity line with a R^2 of 0.9684. The outstanding model performance indicates its capability in exploring the diameter of printed product in new materials, which can vastly reduce the time and cost of experiments. The hyperparameters of this KRR model can be investigated in Supp. Table 3 in Supplemental Information. For the filament case, AgNW, field's metal, PEDOT:PSS, and AgNP were all investigated by ML as new material, but none of the models presented a prominent performance ($R^2 > 0.9$). This may arise from limitations in ML, as each material has one or more features beyond the range of corresponding features in the training set (see Supp. Table 4 in Supplemental Information). For example, in the case of field's metal, the surface tension is 417 dyn/cm which is outside the range

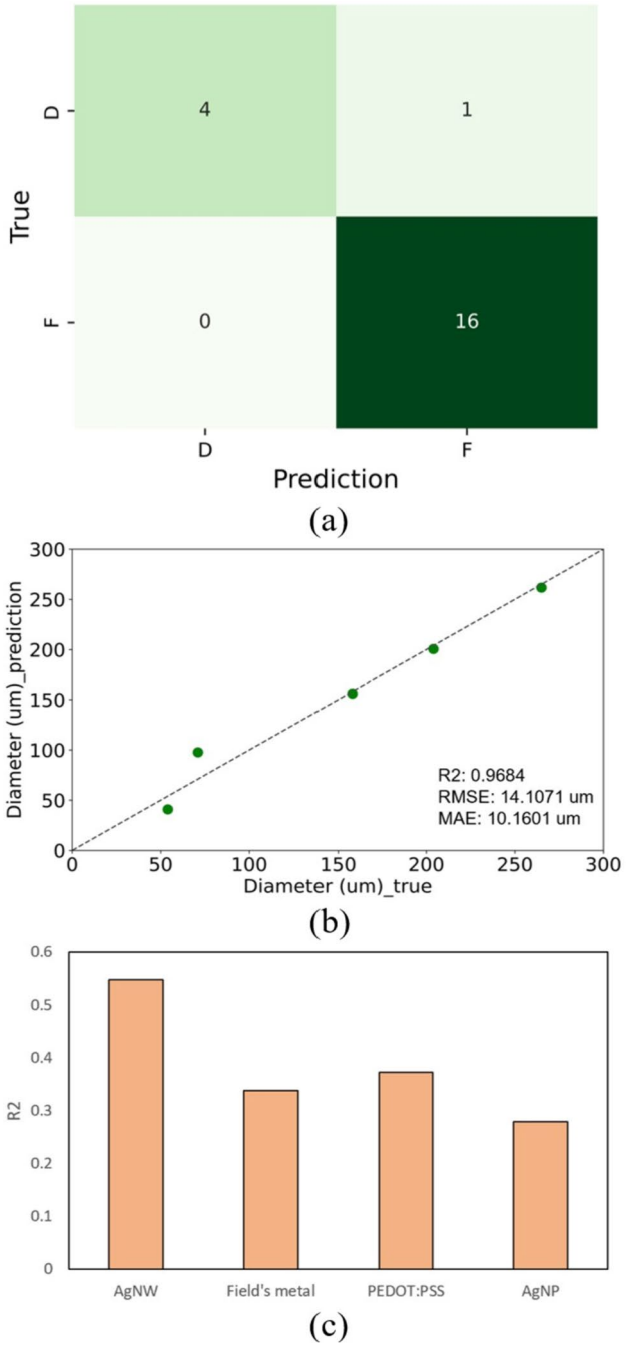

Fig. 6 ML predictions for new material. **a** Classification prediction for PMMA and AgNP (droplet or filament); **b** regression prediction for PMMA (diameter of droplet); **c** R^2 in regression prediction for diameter of filament

of surface tension (30.8–50.8 dyn/mm) within the training set. Similarly, AgNW, PEDOT:PSS, and AgNP, all include features which are outside the range within the training set. Hence, a part of the feature space of the new material has not been explored by the trained model, which drastically deteriorates the model's performance. Figure 6c lists R^2 values for these materials. AgNW only has one parameter, printing speed, which is beyond the range of printing speed in the training set. Referred to Fig. 4c, printing speed is not a significant parameter that affects filament diameter. As a result, it has a higher R^2 and better model performance compared to the other three materials. The R^2 for AgNW is still less than 0.6, with only one feature outside the training set's range, which was ranked high in feature importance. This observation originates from the clustering of samples from the training set in the feature space. In the case of the electric field, which is the most significant feature in controlling filament diameter, the samples are distributed at 2.5 V/μm, in 4.85–5.44 V/μm, 14.45–18.18 V/μm, and 30–60 V/μm. However, the electric filed of the AgNW sample is 20 V/μm, which directs the test samples in a local feature space without data distribution. ML model accuracy depends on the features' input to the model, as well as the data distribution in the feature space. The uneven distribution of samples in the feature space leads to a notable uncertainty when predicting new materials [75]. In the future, the model may be improved by collecting additional samples from literature, as well as experiments. This result highlights the substantial challenge of predicting jetting mode and diameter of printed materials with ML, when the ML model has never encountered such information before. The accuracy of the prediction in diameter decreases as the total number of important features outside the training range increases.

4 Conclusion

In this research, ML models were developed to study the EHD printing process and the interaction between printing and material parameters when determining printing behavior and feature size. By leveraging the ML approach, the importance of process parameters and material properties in determining printing behavior and feature size have been identified with less time and effort using trained random forest models. Besides the factors determined by conventional experiments (viscosity, surface tension, and electric field), the feature importance analysis also demonstrated additional factors (materials' density, etc.) play a significant role in controlling EHD printing behavior. This observation enhances our understanding of the EHD printing mechanisms. Moreover, the developed ML models are capable of predicting jetting mode and feature diameters with good performance in both random train/test split as well as predicting the printing behavior of new materials. The jetting mode was predicted by SVM models with high accuracy and the diameters of printed materials were estimated by KRR models with precision. These findings demonstrate ML's capability for accelerating process design and reducing the number of experiments needed for new materials during EHD printing.

This work provides a new perspective on the research on printing behavior in EHD printing: in need of a subset of empirical samples that varies in material properties and printing parameters, ML can guide research in a more time- and cost-effective direction, without undertaking extensive *trial-and-error* approach-based experimentation.

These models exhibit high accuracy in predicting the jetting behavior and feature size, but limitations still exist. As for future work, more droplet samples can be generated or added to the model, in order to provide more information and enhance the model's predictive performance for droplets. Second, the prediction of filament diameter in new materials faces challenges when no material candidate in the test case has features that entirely fit within the training set, resulting in an inaccurate prediction. In the future, a physics-informed ML model can be developed by adding fundamental science into the standard ML model to overcome this limitation. Lastly, with the future integration of physics-based models and camera images, ML approaches can better assess the printability of new materials and optimize printing results with fewer defects.

Supplementary Information The online version contains supplementary material available at https://doi.org/10.1007/s00170-025-15064-2.

Author contributions All authors contributed to the study conception and design. Material preparation, and experiments were performed by Yiwei Han, James Treadway and Prashant Ghimire. The machine learning was performed by Yizhou Lu. The data analysis was done by Yiwei Han, Samrat Choudhury and Yizhou Lu. The first draft of the manuscript was written by Yiwei Han and Yizhou Lu. Yiwei Han, Samrat Choudhury and Yizhou Lu commented on previous versions of the manuscript. All authors read and approved the final manuscript.

Funding Dr. Samrat Choudhury was financially supported by the National Science Foundation Award number: 2150816. Yizhou Lu has been partially supported by a Graduate Fellowship from the Institute of Data Science, University of Mississippi.

Declarations

Competing interests The authors declare no competing interests.

References

1. Wong KV, Hernandez A (2012) A review of additive manufacturing. Int Sch Res Notices 2012(1):208760
2. Gibson I et al (2021) Additive manufacturing technologies, vol 17. Springer
3. Stavropoulos P (2023) Additive manufacturing: design, processes and applications. Springer Nature
4. Stavropoulos P et al (2024) Addressing the challenge of process stability control in wire DED-LB/M process. CIRP Ann
5. Leach R, Carmignato S (2020) Precision metal additive manufacturing. CRC Press
6. Shulunov VR (2016) Several advantages of the ultra high-precision additive manufacturing technology. Int J Adv Manuf Technol 85:1941–1945
7. Li D et al (2018) Printable transparent conductive films for flexible electronics. Adv Mater 30(10):1704738
8. Ren P, Dong J (2023) Direct printing of conductive polymer PEDOT: PSS for foldable transient electronics. Manuf Lett 35:215–220
9. Zolfaghari A, Chen T, Allen YY (2019) Additive manufacturing of precision optics at micro and nanoscale. Int J Extreme Manuf 1(1):012005
10. Park J-U et al (2007) High-resolution electrohydrodynamic jet printing. Nat Mater 6(10):782–789
11. Bikas H, Stavropoulos P, Chryssolouris G (2016) Additive manufacturing methods and modelling approaches: a critical review. Int J Adv Manuf Technol 83:389–405
12. Xia Y, Whitesides GM (1998) Soft lithography. Angew Chem Int Ed 37(5):550–575
13. Wilkinson N et al (2019) A review of aerosol jet printing—a non-traditional hybrid process for micro-manufacturing. Int J Adv Manuf Technol 105:4599–4619
14. Stavropoulos P, Foteinopoulos P (2018) Modelling of additive manufacturing processes: a review and classification. Manuf Rev 5:2
15. Lee KS et al (2006) Recent developments in the use of two-photon polymerization in precise 2D and 3D microfabrications. Polym Adv Technol 17(2):72–82
16. Jaworek A, Krupa A (1999) Jet and drops formation in electrohydrodynamic spraying of liquids. A systematic approach. Exp Fluids 27(1):43–52
17. Kwon H-j et al (2021) Overview of recent progress in electrohydrodynamic jet printing in practical printed electronics: focus on the variety of printable materials for each component. Mater Adv 2(17):5593–5615
18. Onses MS et al (2015) Mechanisms, capabilities, and applications of high-resolution electrohydrodynamic jet printing. Small 11(34):4237–4266
19. Zhang B et al (2016) Micro/nanoscale electrohydrodynamic printing: from 2D to 3D. Nanoscale 8(34):15376–15388
20. Lee A et al (2013) Optimization of experimental parameters to determine the jetting regimes in electrohydrodynamic printing. Langmuir 29(44):13630–13639
21. Scheideler WJ, Chen C-H (2014) The minimum flow rate scaling of Taylor cone-jets issued from a nozzle. Appl Phys Lett 104(2)
22. Hartman RP et al (2000) Jet break-up in electrohydrodynamic atomization in the cone-jet mode. J Aerosol Sci 31(1):65–95
23. Hartman R et al (1999) Electrohydrodynamic atomization in the cone–jet mode physical modeling of the liquid cone and jet. J Aerosol Sci 30(7):823–849
24. Hartman R, Marijnissen J, Scarlett B (1997) Electro hydrodynamic atomization in the cone-jet mode. A physical model of the liquid cone and jet. J Aerosol Sci 1001(28):S527–S528

25. Choi HK et al (2008) Scaling laws for jet pulsations associated with high-resolution electrohydrodynamic printing. Appl Phys Lett 92(12)
26. Chen C-H, Saville D, Aksay IA (2006) Scaling laws for pulsed electrohydrodynamic drop formation. Appl Phys Lett 89(12)
27. Lee S-H, Nguyen XH, Ko HS (2012) Study on droplet formation with surface tension for electrohydrodynamic inkjet nozzle. J Mech Sci Technol 26:1403–1408
28. Mestel A (1994) The electrohydrodynamic cone-jet at high Reynolds number. J Aerosol Sci 25(6):1037–1047
29. Ganan-Calvo AM (1997) On the theory of electrohydrodynamically driven capillary jets. J Fluid Mech 335:165–188
30. Wei W et al (2012) Numerical simulation of the cone–jet formation and current generation in electrostatic spray—modeling as regards space charged droplet effect. J Micromech Microeng 23(1):015004
31. Pannier CP et al (2017) A dynamical model of drop spreading in electrohydrodynamic jet printing. J Manuf Sci Eng 139(11):111008
32. Du W, Chaudhuri S (2017) A multiphysics model for charged liquid droplet breakup in electric fields. Int J Multiphase Flow 90:46–56
33. Han Y, Wei C, Dong J (2015) Droplet formation and settlement of phase-change ink in high resolution electrohydrodynamic (EHD) 3D printing. J Manuf Process 20:485–491
34. Wei C, Dong J (2014) Development and modeling of melt electrohydrodynamic-jet printing of phase-change inks for high-resolution additive manufacturing. J Manuf Sci Eng 136(6):061010
35. Abbas Z et al (2021) Numerical simulation of electrohydrodynamic jet and printing micro-structures on flexible substrate. Microsyst Technol 27:3125–3139
36. Pan Y, Zeng L (2019) Simulation and validation of droplet generation process for revealing three design constraints in electrohydrodynamic jet printing. Micromachines 10(2):94
37. Shirsavar MA et al (2022) Machine learning-assisted E-jet printing for manufacturing of organic flexible electronics. Biosens Bioelectron 212:114418
38. Ball AK et al (2020) Modeling of EHD inkjet printing performance using soft computing-based approaches. Soft Comput 24:571–589
39. Wang T, Zhou C, Xu W (2019) Online droplet monitoring in inkjet 3D printing using catadioptric stereo system. IISE Trans 51(2):153–167
40. Sun J et al (2019) Electrohydrodynamic printing process monitoring by microscopic image identification. Int J Bioprint 5(1)
41. Oikonomou A et al (2023) Physics-Informed Bayesian learning of electrohydrodynamic polymer jet printing dynamics. Commun Eng 2(1):20
42. Singh SK, Rai N, Subramanian A (2023) Machine learning-informed predictive design and analysis of electrohydrodynamic printing systems. Adv Eng Mater 25(19):2300740
43. Yang YJ et al (2018) Drop-on-demand electrohydrodynamic printing of high resolution conductive micro patterns for MEMS repairing. Int J Precis Eng Manuf 19:811–819
44. Cui Z et al (2018) Electrohydrodynamic printing of silver nanowires for flexible and stretchable electronics. Nanoscale 10(15):6806–6811
45. Kim MW (1997) Surface activity and property of polyethyleneoxide (PEO) in water. Colloids Surf A Physicochem Eng Asp 128(1-3):145–154
46. Han Y, Dong J (2018) Fabrication of self-recoverable flexible and stretchable electronic devices. J Manuf Syst 48:24–29
47. Lipchitz A, Imbert T, Harvel GD (2013) Investigation of fluid dynamic properties of liquid field's metal. In: ASME Power Conference. American Society of Mechanical Engineers
48. Han Y, Dong J (2018) Electrohydrodynamic (EHD) printing of molten metal ink for flexible and stretchable conductor with self-healing capability. Adv Mater Technol 3(3):1700268
49. Wei C, Dong J (2013) Direct fabrication of high-resolution three-dimensional polymeric scaffolds using electrohydrodynamic hot jet plotting. J Micromech Microeng 23(2):025017
50. Chang J et al (2018) Electrohydrodynamic printing of microscale PEDOT: PSS-PEO features with tunable conductive/thermal properties. ACS Appl Mater Interfaces 10(22):19116–19122
51. Lim S et al (2016) Electrohydrodynamic printing of poly (3, 4-ethylenedioxythiophene): poly (4-styrenesulfonate) electrodes with ratio-optimized surfactant. RSC Adv 6(3):2004–2010
52. Nothnagle C et al (2015) EHD printing of PEDOT: PSS inks for fabricating pressure and strain sensor arrays on flexible substrates. In: Next-Generation Robotics II; and Machine Intelligence and Bio-inspired Computation: Theory and Applications IX. SPIE
53. Bae J, Lee J, Hyun Kim S (2017) Effects of polymer properties on jetting performance of electrohydrodynamic printing. J Appl Polym Sci 134(35):45044
54. Guo L et al (2018) Experimental study of the influence of ink properties and process parameters on ejection volume in electrohydrodynamic jet printing. Micromachines 9(10):522
55. Bahrami, A., et al. Dimensionless analysis of the transition from continuous jet mode to natural pulsation in electrohydrodynamic jet printing. in 2023 IEEE Conference on Control Technology and Applications (CCTA). 2023. IEEE.
56. Breiman L (2001) Random forests. Mach Learn 45:5–32
57. Hastie T et al (2009) The elements of statistical learning: data mining, inference, and prediction, vol 2. Springer
58. Breiman L (2017) Classification and regression trees. Routledge
59. Vapnik V (2013) The nature of statistical learning theory. Springer science & business media
60. Vapnik V (1998) Statistical learning theory, vol 2. John Wiley & Sons google schola, pp 831–842
61. Huang M-W et al (2017) SVM and SVM ensembles in breast cancer prediction. PLoS One 12(1):e0161501
62. Huang S et al (2018) Applications of support vector machine (SVM) learning in cancer genomics. Cancer Genomics Proteomics 15(1):41–51
63. Zeng N et al (2018) A new switching-delayed-PSO-based optimized SVM algorithm for diagnosis of Alzheimer's disease. Neurocomputing 320:195–202
64. Chen H-L et al (2011) A support vector machine classifier with rough set-based feature selection for breast cancer diagnosis. Expert Syst Appl 38(7):9014–9022
65. Wu X, Zhao P (2020) Predicting nuclear masses with the kernel ridge regression. Phys Rev C 101(5):051301
66. Tang L, Zhang Z-H (2024) Nuclear charge radius predictions by kernel ridge regression with odd–even effects. Nucl Sci Tech 35(2):19
67. Moreno-Salinas D et al (2019) Modelling of a surface marine vehicle with kernel ridge regression confidence machine. Appl Soft Comput 76:237–250
68. Hoerl AE, Kennard RW (1970) Ridge regression: biased estimation for nonorthogonal problems. Technometrics 12(1):55–67
69. Saunders, C., A. Gammerman, and V. Vovk, Ridge regression learning algorithm in dual variables. 1998.
70. An S et al (2014) Effect of viscosity, electrical conductivity, and surface tension on direct-current-pulsed drop-on-demand electrohydrodynamic printing frequency. Appl Phys Lett 105(21)
71. Barbieri A et al (2004) Static and dynamic density effects due to the finite length of polymer chains: a molecular-dynamics investigation. J Phys Condens Matter 16(36):6609
72. Kraemer EO, Natta FV (2002) Viscosity and molecular weights of polymeric materials. J Phys Chem 36(12):3175–3186

73. Wang F et al (2022) Machine learning predicts electrospray particle size. Mater Des 219:110735
74. Cloupeau M, Prunet-Foch B (1994) Electrohydrodynamic spraying functioning modes: a critical review. J Aerosol Sci 25(6):1021–1036
75. Hwang M, Jeong Y, Sung W-K (2021) Analysis of learning influence of training data selected by distribution consistency. Sensors 21(4):1045